Applied Surface Science 643 (2024) 158653

Contents lists available at ScienceDirect

Applied Surface Science

journal homepage: www.elsevier.com/locate/apsusc

Full Length Article

Engineering multiple defect sites on ultrathin graphitic carbon nitride for efficiently photocatalytic conversion of lignin into monomeric aromatics via selective C–C bond scission

Mengyu Cao [a,1], Shibo Shao [b,c,1], Wenjing Wei [c], Jason B. Love [d], Zongyang Yue [c], Yiming Zhang [e], Xiaolei Zhang [f], Yuxiang Xue [c], Jialin Yu [c], Xianfeng Fan [c,*]

[a] SINOPEC (Beijing) Research Institute of Chemical Industry Co., Ltd., Beijing 100013, China
[b] Petrochemical Research Institute, PetroChina Company Limited, Beijing 102206, China
[c] Institute for Materials and Processes, School of Engineering, The University of Edinburgh, Edinburgh EH9 3BF, UK
[d] School of Chemistry, The University of Edinburgh, Edinburgh EH9 3FJ, UK
[e] School of Materials Science and Engineering, Lanzhou University of Technology, Lanzhou 730050, China
[f] Department of Chemical and Process Engineering, University of Strathclyde, UK

ARTICLE INFO

Keywords:
C–C bond cleavage
Photocatalysis
Lignin conversion
Graphitic carbon nitride

ABSTRACT

Lignin depolymerisation via photocatalytic cleavage of the selective interunit linkage in lignin could be a sustainable approach to produce monomeric aromatic chemicals. However, the insufficient investigation of interunit C–C bond fragmentation has obstructed the rational design of efficient photocatalytic system and further limit the yields of aromatic monomers from lignin depolymerisation. Herein, this work developed the ultrathin g-C_3N_4 with multiple defective sites by simple self-assembly process and in-situ thermal gas-shocking/etching process to catalyse the cleavage of lignin C–C bonds under visible light irradiation. Compared with the pristine g-C_3N_4, the developed g-C_3N_4 photocatalyst exhibited a superior catalytic activity (improved 102 %) and selectivity (~90 %) in the cleavage of C–C bonds in lignin. This study demonstrated that the defects construction and ultrathin structure can optimise the electronic structures of g-C_3N_4 for better separation and transfer of photoinduced charges. And the control experiments and DFT calculation indicated that the created defect sites can promote the generation of essential reactive radicals (e.g., the activation of O_2) and radical intermediates (C–H activation). The present work provides useful insights for the rational use of defect engineering in designing the efficient photocatalytic system for the conversion of lignin into aromatic monomers via the C–C bond cleavage.

1. Introduction

Lignin, which generally accounts for over 15 wt% of lignocellulose, is the only natural aromatic polymer bioresource that is available in large quantities [1–5]. More than 70 million tons of lignin could be generated from papermaking industry and biorefinery every year and the yield of lignin is expected to keep increasing in the future as more biorefineries are coming on stream. However, most of lignin is simply consumed as a low-quality fuel, which is a huge waste and could cause the pollution problem [1,6–9]. Due to the unique natural aromatic structures and the high availability of lignin, lignin is considered as a renewable feedstock to produce value-added functionalised monomeric aromatic compounds via the selective cleavage of interunit linkages between aromatic units in lignin [10–13]. Among all the studies in this research field, since β-O-4 structure is the major form of interunit linkage in natural lignin structures, the depolymerisation of lignin with the production of aromatic monomers through the photocatalytic cleavage of C_β-O linkages between aromatic units in lignin has been intensively studied and obtained significant progresses with the development of various advanced photocatalysts and reaction mechanisms [1,10–14].

However, compared with the intensively studied lignin depolymerisation via C–O bonds scission, the investigation of photocatalytic cleavage of the unneglectable proportion of C–C interunit linkages in lignin are still limited and only a few works focused this area. In fact, the isolated lignin from the conventional lignocellulose fractionation processes and commercial biorefining processes generally contains more

* Corresponding author.
E-mail address: x.fan@ed.ac.uk (X. Fan).
[1] These authors contributed equally to this work.

https://doi.org/10.1016/j.apsusc.2023.158653
Received 28 July 2023; Received in revised form 5 October 2023; Accepted 9 October 2023
Available online 11 October 2023

fractions of C–C bonds as the additional C–C bonds could be formed in the condensation reaction at the expense of C_β–O bonds [1,15]. For example, kraft lignin which is the most common form of technical lignin biomass generated from the paper industry always contains a large amount of recalcitrant C–C bonds instead of C–O bonds due to the lignin degradation and polymerisation processes under harsh alkaline conditions [1,15,16].In this case, the fragmentation of sole C-O linkages cannot fully realise the potential of lignin as a feedstock for producing aromatic compounds. Therefore, even though the fragmentation of C–C bonds is even more challenging than C–O interunit bonds due to the C–C bonds' non-polar properties and robust features in comparison to the C–O bonds (bonding dissociation energy: 288.4–514.1 kJ/mol vs 217.4–334.4 kJ/ mol [17]), it is necessary to investigate the photocatalytic cleavage of the C–C interunit linkage to further improve the yields of monomeric products from lignin depolymerisation for the realisation of lignin valorisation. Generally, β-O-4 and β-1 linkage are the most and the second most abundant interunit linkages in most types of lignin biomass. Thus, the C–C bond scission in this study mainly targets the C_α–C_β bonds in these structures and aimes to generate the corresponding monomeric aromatic compounds [18–21].

Graphitic carbon nitride (g-C_3N_4), as a typical metal-free polymeric semiconductor photocatalyst, has shown some potential in the fragmentation of C–C bonds from lignin [19,21–25]. Liu et al., first found that graphitic carbon nitride could be used as the photocatalyst to cleave C–C bonds in lignin model compounds, and it is worth pointing out that the solid-state NMR results and DFT calculations in this study proved that the π−π stacking interactions between the g-C_3N_4 and aromatic molecular structures in lignin model compounds could promote the molecule activation and the essential charge transfer for photocatalytic reactions [19]. However, the photocatalytic performance of g-C_3N_4 could be restrained by its typical inherent limitations, such as the fast photoinduced carriers' recombination, inappropriate band gap structure, and lack of active sites [26]. The construction of surface defects on photocatalysts has been proven to be a promising approach for improving photocatalytic performances [27]. In the previous studies, various forms of surface defects including surface vacancies (C and N vacancies) and surface functional groups (e.g., –C≡N, –OH, and –NH_2) have been successfully introduced to g-C_3N_4, which led to significant improvements in the selectivity and activity of photocatalytic reactions [26–30]. Besides the intrinsic effects of these defect sites on light absorption and photogenerated carrier separation, these defect sites can also act as the active sites and participate in the corresponding surface reactions. For example, it has been reported that the N defects can effectively adsorb O_2 and promote O_2 activation, and C defects can enhance the redox capability and improve the catalytic activity [27,31]. Notably, the previous studies on the photocatalytic C–C bond scission in lignin indicated that the participation of O_2-derived radicals and the activation of the C–H bond are very crucial in this process. It is reasonable to expect that the construction of defects on graphitic carbon nitride could be a promising approach to improve its catalytic activity for C–C bond fragmentation [18,21,32].

Based on the above expectations, the ultrathin g-C_3N_4 integrated with in-situ formed multiple defects were prepared by a novel facile thermal polymerisation of the supermolecules formed by urea and dicyandiamide with the assistance of thermal gas-shocking etching and exfoliation. The existence of various defects on g-C_3N_4 has been verified by the corresponding characterisation results. And more importantly, the obtained optimised catalyst with multiple vacancies exhibits significantly enhanced performance in the cleavage of C–C bond in lignin model compounds under visible light illumination. Overall, the results and insights of this work present a promising approach to designing metal-free heterogeneous g-C_3N_4 photocatalysts for converting lignin to aromatic monomers via C–C bond cleavage.

2. Experimental section

2.1. Materials

All the chemical reagents used for the synthesis of catalysts were analytic grade and used as received without further purification. Dicyandiamide (99.5 %) and Urea (99.5 %) were purchased from ACROS organics. The monomeric aromatics including Phenol (>99.5 %), Benzaldehyde (>99 %) and Phenyl Formate (>98 %) used for quantitative calibration analysis were purchased from Sigma-Aldrich Co., Ltd. 2-Phenoxy-1-phenylethanol (PP-ol) and 2-phenoxyacetophenone (PP-one) were purchased from Fluorochem Ltd. And other lignin model compounds were purchased from BLD Pharmatech Ltd. unless otherwise stated. Kraft lignin was the by-product from a local paper factory and processed from corn stalk. Ethanol (Absolute, ≥99.8 %) and Acetonitrile (99.9 %) were purchased from Fisher Scientific International, Inc. Argon (zero grade) used for calcination process, Helium (CP grade) and Oxygen (zero grade) used for reaction atmosphere were purchased from the BOC limited. Deionized (DI) water was purified by a CENTRA® R200 Centralized Purification and Distribution Systems.

2.2. Preparation of catalysts

The g-C_3N_4 nanosheets were synthesised by a typical thermal polymerisation process. A certain total amount (10 g) mixture of dicyandiamide and urea with various weight ratios (dicyandiamide: urea = 0.5:9.5, 1:9, 2:8, 3:7) were added into 20 mL DI water and dissolved at 60 °C under magnetic stirring. The solution was kept stirring and dried at 60 °C until the supramolecular precursor of urea and dicyandiamide could be obtained. Then, the supramolecular precursor was grinded into powders and placed in a 50 mL crucible with lid. The crucible with lid was further wrapped with aluminium foil and placed into the centre of a muffle furnace. The furnace was subsequently heated to 550 °C with a ramping rate of 5 °C/min and kept at 550 °C for 2 hr. After naturally cooling down to room temperature, the products were collected and named as $D_xU_{10\text{-}x}$-1 (x = 0.5, 1, 2, 3). Afterward, the grounded samples (250 mg) after the first-time calcination were placed in a ceramic crucible (20 mL) with lid for the second-time calcination in a tube furnace and heated to 550 °C for 2 hr with a heating rate of 5 °C/min under argon atmosphere (Ar flowrate is 120 mL/min). After cooling to room temperature, the obtained products after second calcination were named as $D_xU_{10\text{-}x}$-2 (x = 0.5, 1, 2, 3).

In order to further modify the structure characters of the carbon nitrides, various amount of DI water (5 g, 10 g, 15 g and 20 g) was added into the crucible before the first-time calcination in muffle furnace. In this case, the obtain samples were named as $W_nD_xU_{10\text{-}x}$-1 or $W_nD_xU_{10\text{-}x}$-2, depending on the amount of added water (n = 5, 10, 15, 20) and the times of calcination.

2.3. Characterisation

The crystal phases of g-C_3N_4 were analysed by an X-ray diffractometer (XRD, Phaser-D2, Bruker) with Cu Kα X-ray source at the voltage of 40 kV and current of 40 mA. The optic morphologies and structures of catalysts were imaged by scanning electron microscopy (SEM, Zeiss Sigma VP). Also, the elemental compositions of C, H, N in the samples were measured on an organic elemental analyser (Carlo Erba NA 2500). The infrared (IR) transmission spectra were obtained from a Fourier transform infrared spectrometer (FITR, Shimadzu IRTracer-100) equipped with the DLATGS detector and a KBr pellet was used as the standard The BET (Brunauer, Emmett and Teller) surface area of each prepared sample was analysed by a Quantachrome IQ advanced micropore size and chemisorption analyser at 77 K. The diffuse reflectance UV/Vis spectroscopic (DRS) measurements were conducted on a UV–vis spectrophotometer (Shimazu, UV-3600plus) equipped with a praying mantis accessory (Harrick Scientific) in the spectral range of

200–900 nm using BaSO4 powders as the reflectance standard. The chemical states of each element in prepared catalysts and X-ray photoelectron valence band spectra (XPS-VB) were characterised on an X-ray photoelectron spectrometer (ThermoFisher K-Alpha) with an Al Kα X-ray source. The Solid-state 13C MAS NMR spectra were measured on Bruker Avance III spectrometer with a 9.4 T superconducting magnet. The electron paramagnetic resonance (EPR) spectra of the samples were measured by Bruck A300 spectrometer.

2.4. Computational details

The Quantum Espresso package was employed to perform density functional theory (DFT) calculations within the generalized gradient approximation (GGA) in form of Perdew-Burke-Ernzerhof (PBE) formulation as the treatment of electron exchange and correlation [33–35]. The projected augmented wave (PAW) potentials are used to describe the ionic cores and inner electrons with kinetic energy cutoffs of 45 Ry and 450 Ry, respectively [36,37]. A gaussian smearing of 0.01 Ry was used on the partial occupancies of the Kohn−Sham orbitals. And the geometry optimisation was assumed to be convergent when the force change was smaller than 5×10^{-4} Ry/Bohr. The dispersion interactions were described with Grimme's DFT-D3 methodology. The Brillourin zone was sampled with a gamma-centred grid $3 \times 3 \times 1$ during the computational process. All the plots related to the calculations in this study were visualised with the VESTA software [38].

The molecular structures of g-C_3N_4 were constructed and modified on Materials Studio software [39]. And the unsaturated positions on N atoms at the edge were saturated by H atoms. The equilibrium lattice constants of rectangular g-C_3N_4 monolayer unit cell were optimised (where a = 16.177 Å, b = 12.338 Å) with a vacuum layer of 20 Å to separate the surface slab from its periodic duplicates.

The adsorption energy (E_{ads}) of oxygen molecule (A) was defined as:

$$E_{ads} = E_{A/surf} - E_{surf} - E_A$$

$E_{A/surf}$, E_{surf} and E_A represent the energy of substrate adsorbed on the surface, the energy of clean surface and the energy of isolated substrate molecule.

2.5. Photocatalytic performance evaluation

A customized quartz reactor with a cooling water jacket was used in this work. A xenon arc lamp (manufactured by Perfect Light Company) equipped with a PE300BF type light bulb and a 420 nm UV filter was used as the light source. The position of the lamp was fixed to ensure the light intensity in different tests were the same, which was about 0.35 W/cm^2 at the centre. Typically, 10 mg of catalyst, 10 mg of lignin model compounds (or the extract from natural plant tissue or the kraft lignin biomass) and 5 mL of CH_3CN were added into the reactor. The mixture could form a well-dispersed suspension with the aid of magnetic stirring. During the reaction process, oxygen, or other gases was bubbled into the reaction solution with 5 sccm of flowrate and the reactor was placed under illumination with magnetic stirring at 300 rpm. The temperature was kept at around 20 °C with the aid of the cooling water system. After the reaction, the catalyst was removed by filtration or centrifugation (10,000 rpm for 10 min). Then, 1 mL supernatant liquid was taken out and mixed with 4 mg of methylparaben as the internal standard. Next, the mixture solution was diluted by a factor of 50 times with acetonitrile. The conversion of lignin model compounds and the yields of aromatic monomer products were identified and quantified by gas chromatography-mass spectrometry (GC–MS, QP2010 SE, Shimadzu) and the column used in this work is RXI-5MS Cap Column 30 m, 0.25 mm ID, 0.25 μm.

The following operation parameters were generally applied to the GC–MS: injection temperature: 280 °C; column temperature program: 80 °C for 2 min, then increasing the temperature to 270 °C at a rate of 10 °C/min, then heat up to 300 °C at a rate of 30 °C/min and holding the temperature for 5 min, The scanning speed of MS is 1000, starting from 45 *m/z* and end at 220 *m/z*.

The conversion rate of lignin model compounds, selectivity and yield of products are calculated based on the following equations:

$$\text{Conversion\% (Reactant)} = 1 - (\text{Residual Reactant} / \text{Initial Reactant}) \quad (1)$$

$$\text{Selectivity\% (Product)} = \text{Mole of Product Formed} / \text{Mole of Reactant Converted} \quad (2)$$

$$\text{Yield\% (Product)} = \text{Selectivity\% (Product)} \times \text{Conversion\% (Reactant)} \quad (3)$$

3. Results and discussion

3.1. Synthesis of defective g-C_3N_4

The schematic diagram of the preparation of defective g-C_3N_4 is shown in Scheme 1 and the detailed stoichiometric information could be found in section 2.2. In the first step, the dicyandiamide solution was introduced into the urea solution to form a supramolecular composite via the hydrogen-bond assisted self-assembly process [40]. The g-C_3N_4 was attained by the thermal polymerisation process. In the subsequent material preparation process, the addition of water was used to promote the generation of endogenous gaseous species (e.g., NH_3, H_2O and CO_x) during the heating process, resulting in the formation of defects and the change of the packed layer structure in g-C_3N_4 by thermal gas-shocking exfoliation effect during the polymerisation process of g-C_3N_4 [27,29,31]. After the 1st step, the obtained samples presented a foam-like architecture, and the yields of samples gradually decreased with the increase of additional water due to the excessive conversion of precursor into endogenous gas (Table S1). The evolution of materials in the first preparing stage is similar to the previous studies in which g-C_3N_4 materials are treated in different atmosphere to introduce different types of vacancies into the g-C_3N_4 structure [31].

The 2nd heat treatment under argon atmosphere could generate more N vacancies on the g-C_3N_4 surface, because argon molecules excited by the enormous amounts of energy at a high-temperature environment can etch the g-C_3N_4 surface by passing the energy exceeds the binding energy [27,41]. Thermogravimetric analysis (TGA) was conducted to evaluate the performance of the 2nd thermal etching treatment, the weight loss of each sample was neglectable before heated up to 500 °C but a significant drop of weight can be observed after 500 °C (Fig. S1). The differences of weight loss between D1U9-1and W10D1U9-1could be attributed to the looser layer stacking structure formed with the addition of water at the first calcination stage. Moreover, as shown in Table 1, the elemental analysis results from X-ray photoelectron spectroscopy (XPS) and organic element analysis (OEA) measurements reveal that the surface and total N/C atomic ratio decreased after the argon heat treatment, which further confirm the formation of N vacancies at this stage [27]. Also, it should be noted that the change of N/C ratio measured on XPS is more significant than it measured by OEA, suggesting that the created defects are mainly formed on the surface.

3.2. Material characterization

The structures of all samples were firstly characterised by X-ray diffraction (XRD) to investigate the crystal phases of prepared samples from different synthesising processes. As shown in Fig. 1 (a), all samples exhibited the typical characteristic XRD peaks of g-C_3N_4 at 13.1° and 27.7° assigned to the (1 0 0) and (0 0 2) planes, which could be respectively indexed to the in-plane packing of heptazine units of g-C_3N_4 and the interlamellar distance of the stacking layers [26,27]. The XRD patterns can confirm that the successful synthesis of g-C_3N_4 from the preparation approach used in this work and the crystal phases of g-C_3N_4

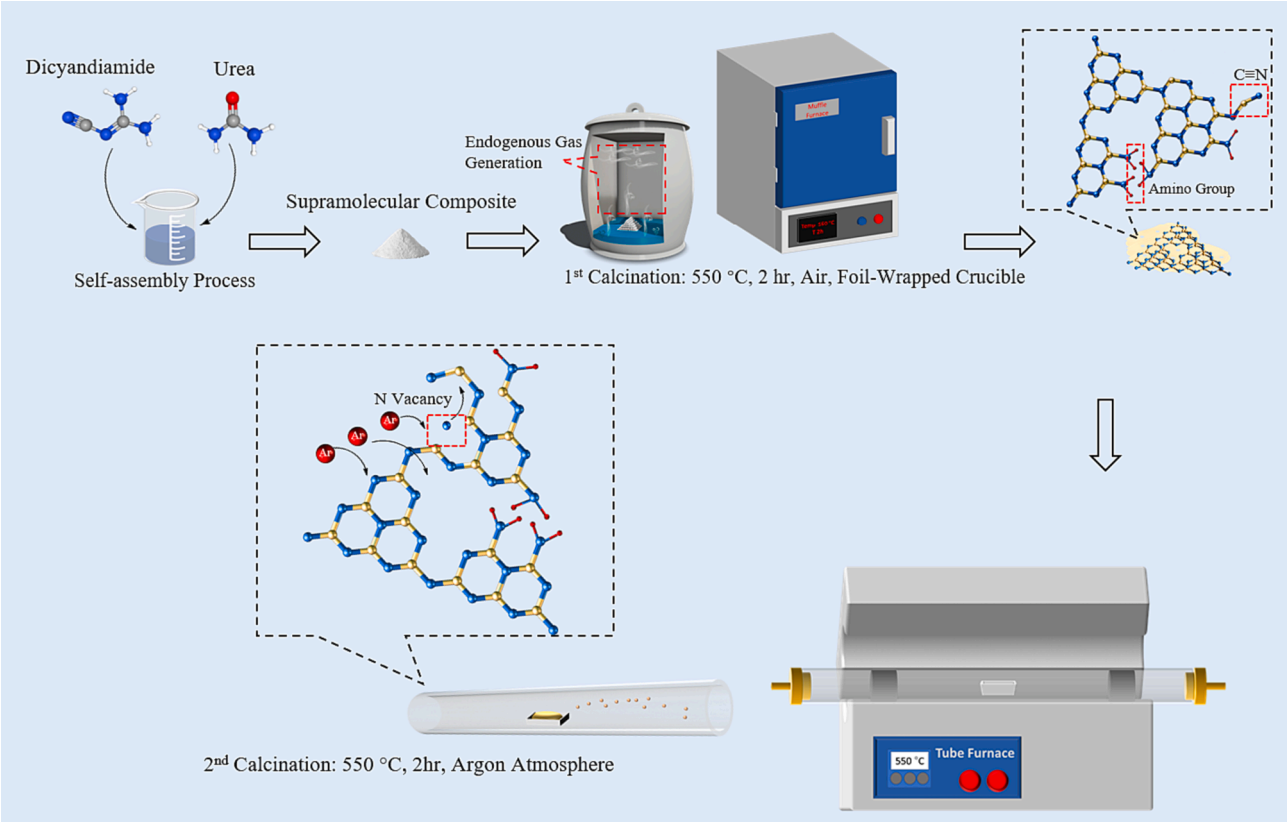

Scheme 1. Schematic illustration of the preparation process of defective g-C_3N_4 in this study.

Table 1
N/C atomic ratio of samples from the elemental composition analysis carried out on XPS and OEA.

Sample ID	N/C atomic ratio (XPS)	N/C atomic ratio (OEA)
U10-1	1.300	1.694
D10-1	1.255	1.697
D1U9-1	1.323	1.676
D1U9-2	1.136	1.675
W10D1U9-1	1.300	1.685
W10D1U9-2	1.053	1.619

could also be retained well during the in-situ thermal gas-shocking process. The diffraction peaks were slightly attenuated with the addition of water at the first synthesis stage and significantly attenuated after argon thermal etching at the second synthesis stage, respectively. These results suggest that the original g-C_3N_4 structures and layered stackings were dismembered and formed defective short-range ordered graphitic molecular fragments [26,27,31].

The morphologies and microstructures of samples were investigated by using scanning electron microscopy (SEM) and atomic force microscopy (AFM). Due to the strong π–π interaction between stacking layers, the pristine g-C_3N_4 made from sole urea or dicyandiamide presents typical hierarchical or bulk morphology characters as displayed in Fig. S2 (a-d), which is consistent with the previous works [31,42,43]. As expected, sheet-like g-C_3N_4 could be observed from D1U9-1, D1U9-2, and W10D1U9-2, and the exfoliated nanosheets could be identified from these samples due to the in-situ exfoliation effect during the material formation process (Fig. S2 e-j). Among, W10D1U9-2 exhibited more fully exfoliated small nanosheets and the thickness of the nanosheets was measured by AFM. As shown in Fig. S3 (a-f), the thickness of the nanosheets in W10D1U9-2 is only around 1 nm or less than 1 nm in comparison to around 6 nm of thickness for the nanolayers in bulk g-C_3N_4 (U10-1). The optical observation of the prepared samples can further prove that the morphologies of the original g-C_3N_4 structure could be controlled by the proposed synthesis procedure in this study and the fragmented smaller and thinner nanosheets could be obtained with the formation of supramolecular composites and the addition of water.

Moreover, as shown in Fig. S4 (a, b), all samples exhibit the typical type-IV patterns with the H3 hysteresis loop in the N_2 adsorption–desorption isotherms, confirming the formation of slit-shaped pores and the non-rigid aggregates of plate-like particles in the samples [31,44,45]. The results of the N_2 physisorption measurements and the pore size distribution show that the formation of supermolecule, the 2nd thermal etching treatment and the adding of water can significantly modify the surface and pore structure of g-C_3N_4. Therefore, the optimised sample W10D1U9-2 has a larger BET specific surface area and more pore volume in comparison to the pristine g-C_3N_4 synthesised from sole urea or dicyandiamide (96.764 m^2/g vs ~ 40 m^2/g; 0.452 cc/g vs ~ 0.15 cc/g). These results indicate that the thinned and exfoliated nanosheets can expose more active sites and reduce the diffusion distance of the photogenerated charges, which could be beneficial to photocatalytic activity [42].

Fourier transform infrared (FTIR) spectra was employed to probe the chemical structural changes in different samples from different treatments. As shown in Fig. 1 (b), all samples present similar characteristic peaks in the region of 790–810 cm^{-1}, 1200–1700 cm^{-1} and 2900–3300 cm^{-1}, which could be identified as the out-of-plane bending mode of heptazine rings, the stretching modes of aromatic C-N heterocycles, and the stretching vibrations of the amino group (–NH_x), respectively [26,27,31,46]. Specifically, the peaks at approximately1410, 1490, 1570, 1650 cm^{-1} come from the stretching vibrations of heptazine-derived repeating units and the peaks at around 1250 and 1340 cm^{-1} corresponds to the bending vibrations characteristic of heptazine rings, which is consistent with the FTIR analysis of the g-C_3N_4 [47,48].

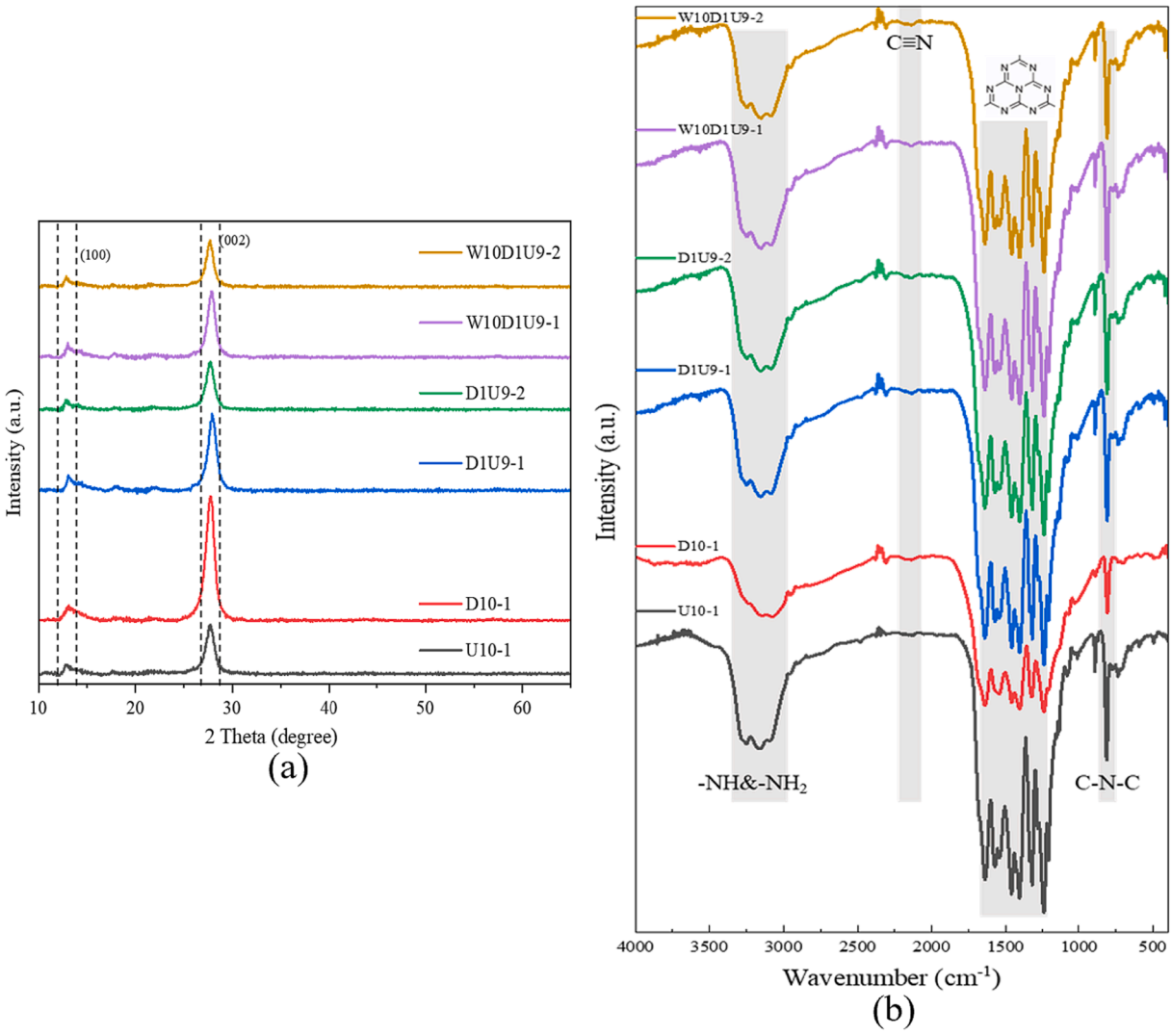

Fig. 1. (a) The XRD patterns of representative prepared samples; (b) The FTIR spectra of prepared samples.

Compared with pristine g-C_3N_4 synthesised from sole urea, the stretching vibration of the cyano group (–C≡N) could be identified at around 2150–2200 cm^{-1} from the rest of samples and could be maintained after argon heat treatment [26,27]. The formation of cyano group may be ascribed to the deprotonation of the C-NH_2 groups with the endogenous gas during thermal polymerisation process [27,31]. Solid-state ^{13}C magic angle spinning nuclear magnetic resonance (MAS-NMR) technique was used to further determine the detail changes of the heptazine structure. As shown in Fig. S5, the NMR spectra of pristine g-C_3N_4 and W10D1U9-2 both display two strong peaks at 164.9 ppm and 173.2 ppm, which respectively originated from C(1) atoms of N=C-N_2 and C(2) atoms of N=C–N(NH_x) in the heptazine units [46]. Also, the new peaks at around 117.5 ppm from W10D1U9-2 could be identified as the C atoms in the cyano group, which further confirmed the existence of cyano group in the structure [27,46].

In addition, X-ray photoelectron spectroscopy (XPS) is used to determine the chemical states of C and N elements for further investigating the formation of defective structures. As the XPS survey spectra shown in Fig. 2 (a), all samples are mainly constituted of C and N with a neglectable amount of O at an approximately binding energy of 288 eV, 398 eV and 531 eV, respectively [42]. As for high-resolution XPS spectra of C1s (Fig. 2 (b)), four main fitting peaks could be identified at around 284.8 eV, 286.8 eV, 288.4 eV and 289.2 eV, which could be ascribed to adventitious carbon (C_1), the carbon (C_2) in C-NH_x groups (x = 1, 2), the tertiary carbon (C_3) in N–C=N in the aromatic rings of the g-C_3N_4 heterocycles and =CNH_2 groups (C_4) [26,31,49]. It should be noted that the C_2 peak positioned at around 286.6 eV arises and gradually increases in D1U9-1, D1U9-2, and W10D1U9-2. Since it is unlikely to form more C–NH_x groups in this case and C≡N groups and C-NH_x groups have the similar binding energies, the increased C_2 peak indicates that the formation of C≡N groups from dehydrogenation of the C–NH_X groups [27]. Moreover, the area ratio of C_3 to the total carbon peaks exhibit a decreasing trend and W10D1U9-2 has the lowest value (Table 2), further suggesting that the decomposition of tri-s-triazine structure in g-C_3N_4 and the formation of carbon vacancies on tertiary carbon sites [31]. As shown in Fig. 2 (c), the XPS spectra of N 1s for all samples could also be deconvoluted into four Gaussian peaks at around 398.8 eV, 400.1 eV, 401.2 eV and 404.3 eV, which could be associated with the nitrogen atoms in sp2-hybridised C–N=C structure (N1), tri-coordinated N-$(C)_3$ structure (N2), NH_X groups (N3) in the framework and π excitation effect in heptazine rings (N4), respectively [26,27,42]. The binding energy of N2 peak in W10D1U9-2 was shifted to the lower direction, which could be ascribed as the existence of adjacent N defectives in the structure [27]. Also, for W10D1U9-2, the ratio of N1/N2 decreases to 3.59 while the ratio of N1/C1 also significantly decreases to 1.29, which further reveals the formation of N vacancies in this sample [26,27].

The defective structure of W10D1U9-2 was also investigated by electron paramagnetic resonance (EPR) spectroscopy and U10-1was also

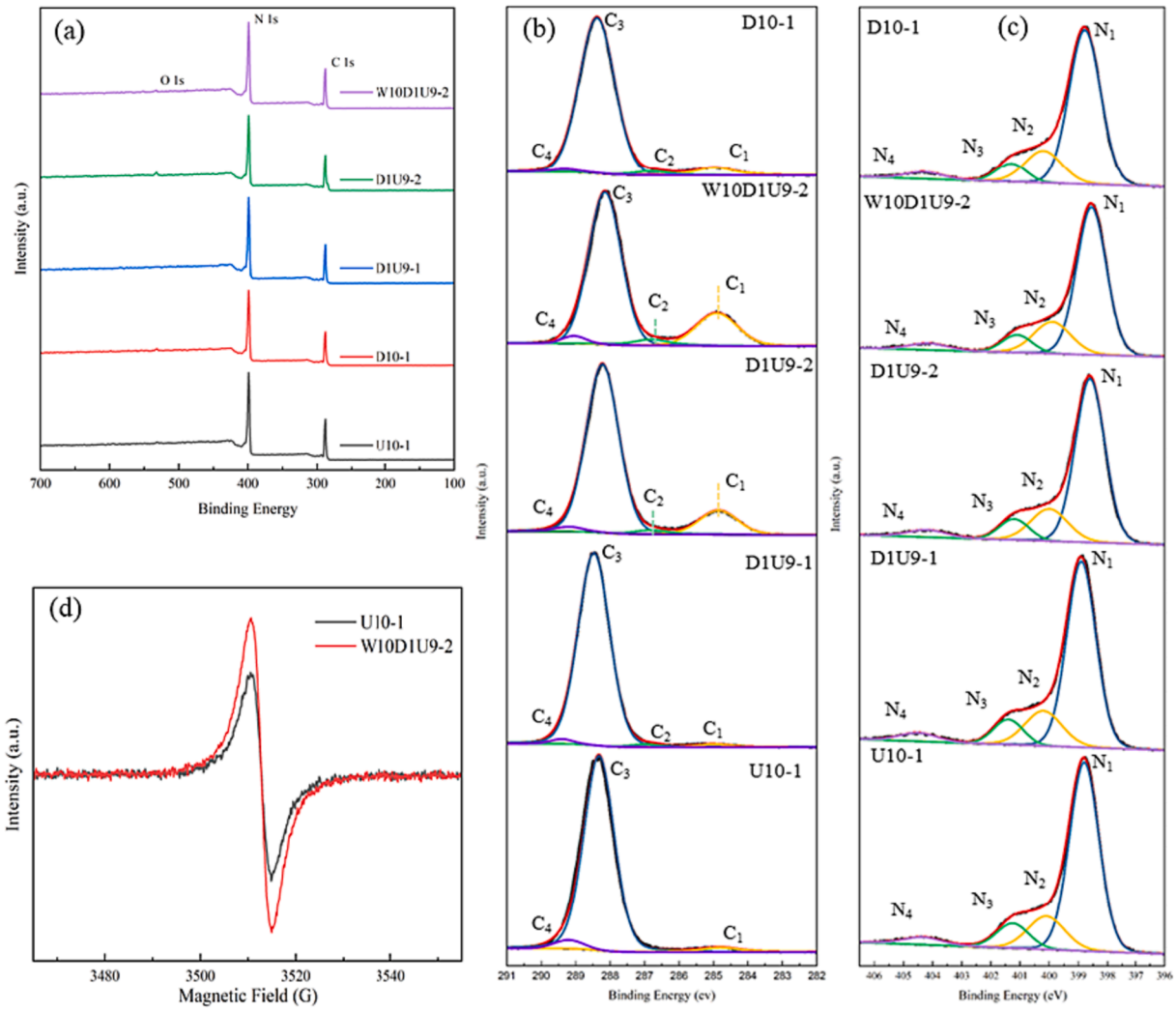

Fig. 2. The XPS survey spectra (a) and high-resolution C 1s (b) and N 1s (c) XPS spectra of prepared g-C_3N_4; (d) EPR Spectra of U10-1 and W10D1U9-2.

Table 2
The area and area fractions of various C/N types on XPS spectra for different samples.

Area Area Fraction	C1	C2	C3	C4	N1	N2	N3	N4
U10-1	1607	–	39588.2	1560	72,944	16,446	10,696	4503
	0.038	–	0.926	0.036	0.697	0.157	0.102	0.043
D1U9-1	795	482	39,484	699	70,217	17,231	9461	4369
	0.019	0.012	0.952	0.017	0.693	0.170	0.093	0.043
D1U9-2	5926	944	35420.6	995	62,877	15,832	7845	3745
	0.137	0.022	0.818	0.023	0.696	0.175	0.087	0.041
W10D1U9-2	9641	1834	31272.5	1156	56,779	15,647	6645	3407
	0.220	0.042	0.712	0.026	0.688	0.192	0.081	0.042
D10-1	2527	1205	34,698	735	62,999	16,141	7040	3647
	0.065	0.031	0.886	0.019	0.701	0.180	0.078	0.041

characterised for comparison. As shown in Fig. 2 (d), due to the unpaired electrons generated by the carbon atoms on the heptazine rings, the same g value (g = 2.004) could be determined from the Lorentz lines of sample U10-1 and W10D1U9-2 [27,31,45]. However, the EPR signal intensity of W10D1U9-2 was not attenuated by the loss of carbon, even though the existence of carbon defects could be proved in this study. The enhancement of EPR signal from pristine g-C_3N_4 to W10D1U9-2 could be mainly due to the strong electron-withdrawing effect of cyano group (–C≡N) and the formation of N vacancies on bi-coordinated N positions [27,45]. In this case, the generation of unpaired electrons could be effectively promoted, which is beneficial to the migration and separation of photogenerated charges and thus resulting in higher photocatalytic activity [27,45,50].

The electronic structure was investigated by UV–Vis diffuse reflectance spectroscopy (DRS) spectra and XPS-VB (valence band) to determine the width and band edges of bandgaps for each sample and further evaluate the light utilisation ability and reduction/oxidation potential of the prepared samples. The DRS spectra (Fig. S6) demonstrates the light absorption properties of samples, and the modified g-C3N4 exhibited good visible light harvesting properties. Compared with U10-1, the red

shift in the intrinsic absorption bands of sample D1U9-1, D1U9-2 and W10D1U9-2 may be related to the $\pi \rightarrow \pi^*$ electron transition of the sp2 hybridization conjugated aromatic rings and the $n \rightarrow \pi^*$ electron transition of the unpair electrons from the defective sites [27,51]. And the blue shift of the light absorption band in W10D1U9-2 in comparison to D1U9-2 could be ascribed to the quantum size effect of ultrathin nanosheet structure [31,42]. The bandgap values were subsequently determined based on Tauc plots and Kubelka-Monk theory, and the valence band values versus standard hydrogen electrode (SHE) were calculated based on valance band edge potential (E_{VB}) from XPS VB spectra with the estimated work function (Φ) of the XPS analyser (4.37 eV) and vacuum level vs SHE (−4.44 eV). Next, the conductive band values could also be determined based on the equation $E_{CB} = E_{VB} - E_{Bandgap}$, and all the information about band alignments were summarised in Table S2. Herein, the narrowed bandgap width and the negative shift of the band alignments could be attributed to the synergistic effect of N/C defects, cyano groups (–C≡N), and the ultrathin nanosheet structure, which is consistent with the literature report [27,31].

Furthermore, the electronic structures and charge density distribution of pristine g-C_3N_4 and g-C_3N_4 with defects were calculated using DFT method respectively, to evaluate the effects of defects on the modification of bandgap structures and the enhancement of the separation of photogenerated carriers. Two models of pristine g-C_3N_4 and g-C_3N_4 with various defects were respectively built as illustrated in Fig. S7, and significant lattice deformation and twisted tri-s-triazine rings could be observed from the defective g-C_3N_4 in comparison to the pristine g-C_3N_4. The plotted density of states of two different g-C_3N_4 indicate that the defects caused the downward shift of CB and resulted in the narrowed bandgap compared to the pristine g-C_3N_4, which is in line with the characterisation results. Moreover, a mid-gap state of approximately 0.9 eV above the valence band appears in g-C_3N_4 with defects (Fig. S8), which can act as the recombination centre contributing to the charged carriers' separation [26]. The corresponding calculated charge density distributions of g-C_3N_4 with or without defects further indicate the positive effect of the created defects on the charge carrier separation efficiency. As shown in Fig. S9, the charge density distributions of pristine g-C_3N_4 are relatively uniform while the modification of the defective structures leads to spatially localised charge density distribution. It has been widely accepted that this type of spatially localised charge distribution could promote the separation of charged carriers and thus facilitate the surface reactions driven by photoinduced holes and electrons [26,27,52].

3.3. The evaluation of photocatalytic performance in C–C bond scission

2-phenoxy-1-phenylethanol (PP-ol) was first employed as the model substrate to evaluate catalytic performance of prepared g-C_3N_4 due to its representative β-O-4 molecular structure and its ready comparison to previous studies [19,22]. As shown in entry 1 and 11 of Table S3, after 5 h visible light irradiation, the pristine g-C_3N_4 from sole precursor (urea or dicyandiamide) showed relatively low photocatalytic activity (~30 %–40 %) for the conversion of PP-ol into monomeric aromatics (Benzaldehyde, Phenyl Formate, and Phenol), which may be owing to their inherent negative material properties for photocatalytic activity including the inappropriate electronic structure, low surface area and lack of active sites. Subsequently, the g-C_3N_4 made from the supermolecule formed by urea and dicyandiamide can significantly increase the conversion rate of PP-ol to 67.6 % with the optimised ratio of dicyandiamide and urea (entry 5, Table S3), but further increasing the amount of dicyandiamide led to a decreasing in photocatalytic activity (entry 7 and 9, Table S3). Otherwise, it was found that the conversion of PP-ol carried on the same g-C_3N_4 catalysts could be increased by about 20 %–25 % after the 2nd heat treatment under the argon atmosphere (entry 2, 4, 6,8, and 10, Table S3). For example, D1U9-2 derived from the D1U9-1 could process over 80 % of PP-ol substrate with over 80 % of selectivity for desirable monomeric aromatic products. Based on the characterisation results, this improvement of photocatalytic activity caused by argon heat treatment could be ascribed to the formation of N vacancies and cyano groups in the structure, which can optimise the electronic structure for better photocatalytic properties and probably also can act as the active sites in the reaction [27].

Based on the above results from the evaluation of photocatalytic activity and material characterisation, it is very likely that the defectives on g-C_3N_4 can promote the cleavage of C–C bonds in PP-ol. Therefore, in order to further improve the photocatalytic activity, water is used as the additive in the synthesis process to promote the generation of endogenous gases and thus further promote the formation of defective structures and construct ultrathin nanosheet morphology [26,31,46]. As shown in Fig. 3 (a), in the beginning, W5D1U9-1 and W5D1U9-2 synthesised with 5 mL of additional water respectively exhibited similar photocatalytic performance with D1U9-1 and D1U9-2. Further increasing the addition of water to 10 mL at the first stage of synthesis process, the obtained samples W10D1U9-1 and W10D1U9-2 displayed significantly improved catalytic activity in comparison to the D1U9-1 and D1U9-2 (The conversion rate of PP-ol: 74.3 % vs 67.6 % and 90.4 % vs 81.5 %, respectively). Combined with the characterisation results, these results suggest that the promoted formation of C/N vacancies could improve the photocatalytic activity in this reaction. However, further increasing the addition of water in the first synthesis stage led to a decrease in the photocatalytic activity for this reaction, suggesting that the over-generation of defects in g-C_3N_4 structures may be detrimental to the catalytic performance.

As a heterogeneous catalyst, W10D1U9-2 could be easily separated from the reaction solvent environment by centrifuge or filtration process. Subsequently, the recyclability test of this catalyst was performed under five consecutive reaction cycles with the identical reaction conditions. As shown in Fig. 3 (b), the differences in the catalytic performance including the reaction rate of the substrate and the selectivity for each product between the fresh and reused catalysts could be neglected, not only strongly confirming that the prepared catalysts in this study are relatively stable for recycling use but also revealing the potential application of this photocatalytic system.

The photocatalytic reaction yield versus reaction time was also evaluated in this work. As shown in Fig. 3 (c), the gradually decreased reaction rate could be ascribed to the decreased concentration of reactants in the batch reactor system. During the entire reaction process, it is worth pointing out that over 80 % selectivity for monomeric aromatic products could be remained whereas the oxy-dehydrogenation of PP-ol to PP-one was kept at a relatively low level. Also, it should be noted that the yield of phenol raised with the approximately same stoichiometric amount of phenyl formate decreased after the extended illumination time to 6 hr, implying the possibility of the transformation from phenyl formate to phenol. The control experiments which directly employed PP-one or phenyl formate as the reactant were also performed to further study the reaction routes. As shown in Scheme 2 (a), the C–C bond cleavage for PP-one is significantly slower than it for PP-ol, which could be explained by the higher bond dissociation energy (BDE) of C–C bonds in ketone compounds [22]. This result is agreeing with the previous studies and indicates that the ketone compounds generated from the oxy-dehydrogenation process are not the intermediate products, instead, this process is a competitive side reaction to the targeting C–C bond fragmentation [19]. Otherwise, as shown in Scheme 2 (b), the sole phenyl formate conversion experiment proved that about 30 % of phenyl formate could be consumed with nearly 90 % of selectivity for phenol, confirming that phenol is generated from the hydrolysis of phenyl formate. Compared with the previously published studies stated that no considerable decomposition of phenyl formate during the whole reaction process, the conversion of phenyl formate into phenol maybe owing to the enhanced redox capability of the prepared g-C_3N_4 in this study, which also resulted in the improved photocatalytic reaction efficiency.

It is very likely that oxygen participates in the reaction of C–C cleavage since the generated product of phenyl formate is formed with

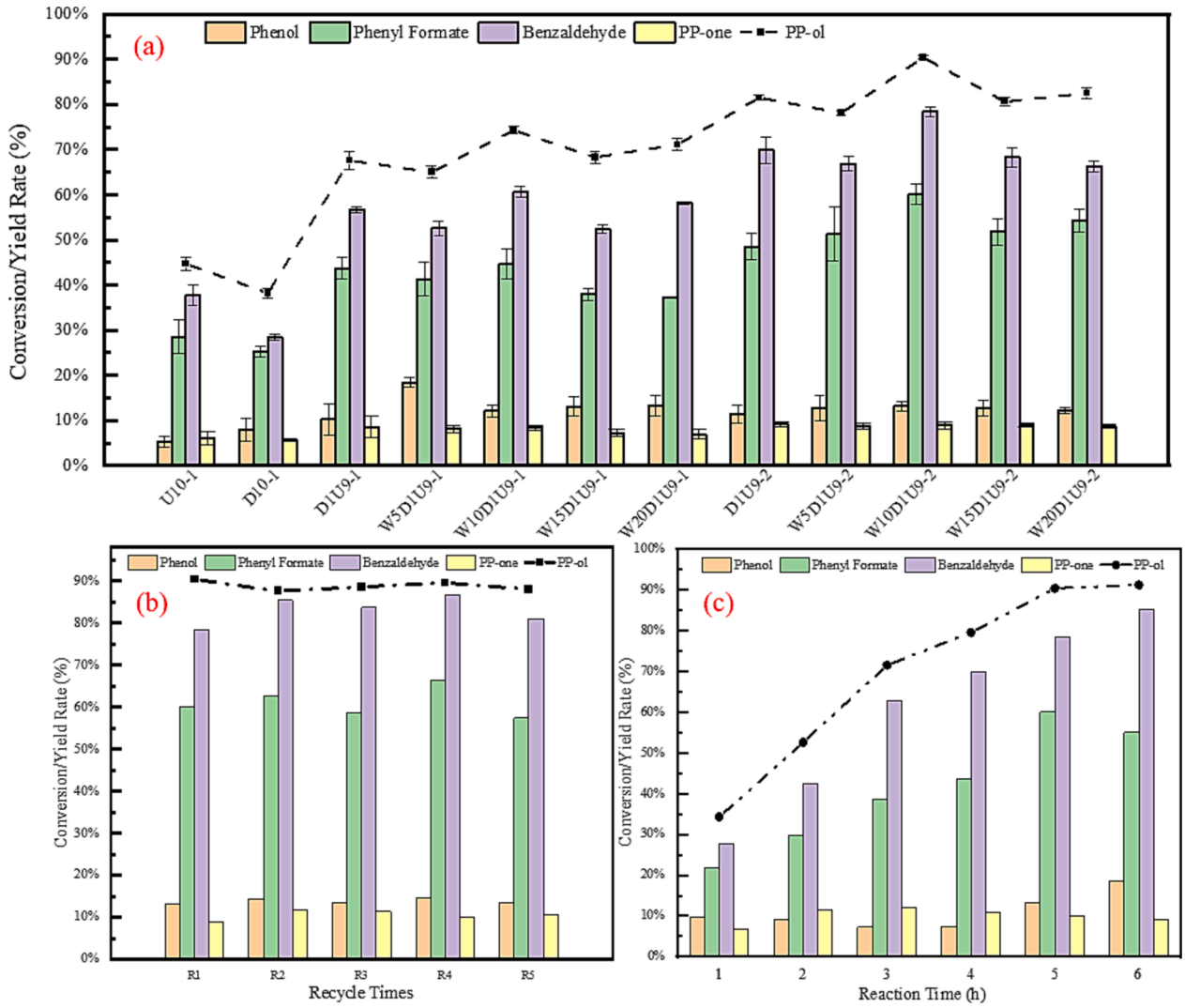

Fig. 3. (a) The conversion of PP-ol under O_2 saturated (1 atm) condition after 5 hr of visible light illumination with modified g-C3N4 catalysts synthesised with different amount of additional water; (b) The reusability test for W10D1U9-2; (c) Time course process W10D1U9-2 for the photocatalytic conversion of PP-ol under visible-light irradiation. Typical reaction condition: 10 mg of PP-ol (~0.05 mmol), 10 mg of catalyst, 5 mL of CH_3CN as the solvent, visible light irradiation (0.35 W/cm^2), room temperature (20–25 °C), 5 hr. The quantitative analysis of each chemical was determined by GC–MS with Methylparaben as the internal standard.

an extra oxygen atom. Therefore, different reaction atmosphere conditions were tested for further understanding of this reaction process. As displayed in Fig. S10, the conversion rate decreased by around 10 % when the oxygen reaction atmosphere was replaced by air condition. Subsequently, this reaction was also conducted under N_2 and He atmosphere, respectively. In these cases, the conversion of PP-ol could be extremely suppressed to below 10 % and only benzaldehyde could be detected from the products, indicating that the reactive oxygen species (ROS) originated from the O_2 could be essential to the reaction of C–C cleavage.

Additionally, 1,2-diphenylethanol (DPol) as the β-1 lignin model compound was employed to examine the applicability of this photocatalytic system. As shown in Scheme 2 (c), DPol could be mainly converted to benzaldehyde via C–C bond dissociation, and around 10 % of 1,2-diphenylethanone (DPone) could be generated as the products from the oxy-dehydrogenation process. And DPone also showed similar nonreactivity as PP-one in C–C cleavage as previously reported [21].

Furthermore, kraft lignin isolated from corn stalks and the extracted lignin from birch wood sawdust were also used as the reaction substrates to further assess the feasibility of this prepared g-C_3N_4 photocatalyst. As shown in Fig. 4, the colour differences between the reaction solution with or without the catalyst after 12 h of visible light irradiation intuitively present the degradation of reaction substrates with the presence of the catalyst. And the subsequent identification and quantitative analysis for yielded products carried on GC–MS further illustrated that the various monomeric aromatic compounds could be generated from the photo-catalysed lignin decomposition process. All these results can strongly prove that the g-C_3N_4 modified by the proposed defective construction strategy is capable to efficiently cleave the interunit C–C bonds and generate monomeric aromatic compounds, and this photocatalytic system may have great potential for realising lignin valorisation via the conversion of lignin biomass into value-added products.

3.4. Reaction mechanism investigation

The scavenger quenching experiments for photoinduced charges and radicals were performed to explore the functions of photoinduced holes/electrons and reactive radicals oriented to the C–C bond cleavage in β-O-4 structure or β-1 structure for further understanding the reaction routes and mechanism. As shown in Fig. 5, the hole scavenger ($Na_2C_2O_4$) can apparently inhibit the conversion of PP-ol (from above 90 % to around 60 %), suggesting that the oxidation of the reactant driven by the photogenerated holes could be very important to the cleavage of C–C bonds in β-O-4 structures. It is worth pointing out that the generation of phenol

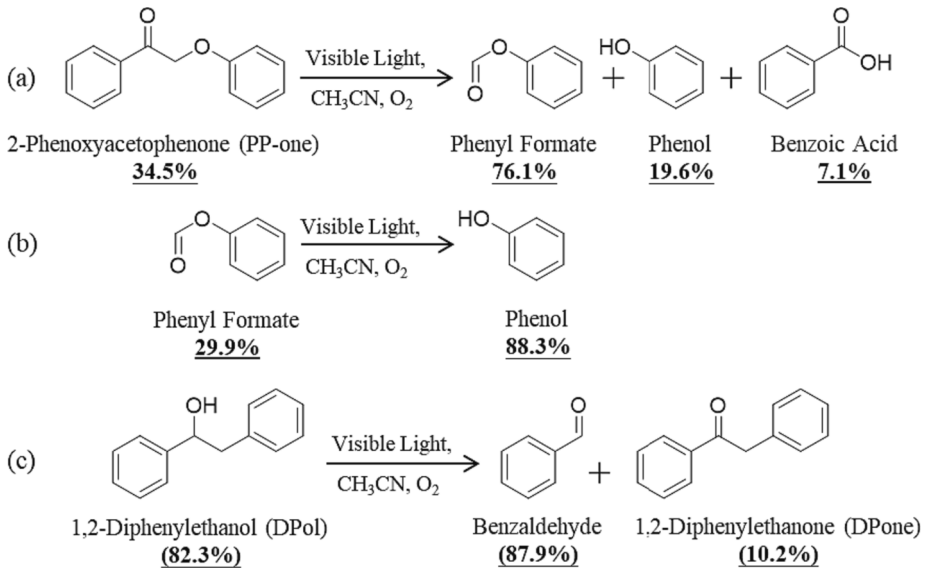

Scheme 2. The control experiments with different reaction substrates (number% represents the conversion rate/yield rate of each compound).

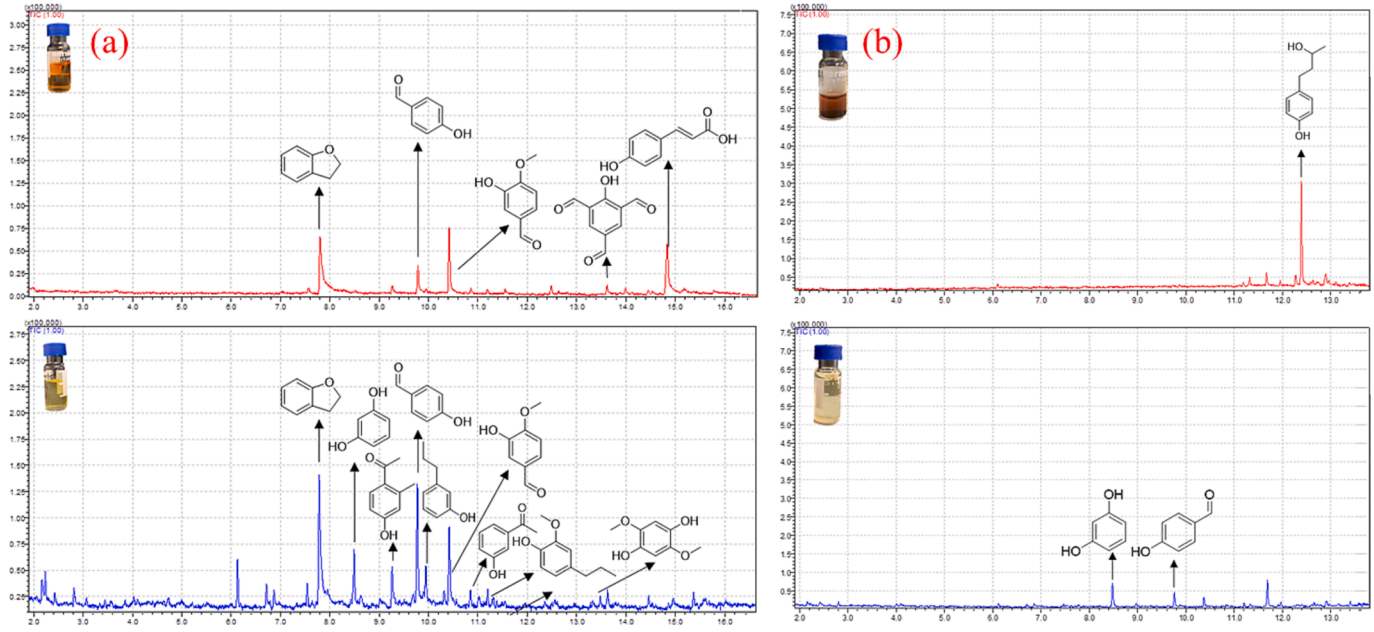

Fig. 4. GC–MS spectra for photocatalytic conversion of (a) kraft lignin and (b) extracted lignin from birch wood. (Red line represents the results from comparison experiments without catalysts and blue line represents the results from the reaction with catalysts) Reaction conditions: 100 mg of Kraft lignin powders, 20 mg of W10D1U9-2, 10 mL of CH_3CN, O_2 atmosphere, visible light irradiation, 12 h.

and PP-one was also supressed by the addition of hole scavenger, indicating that the hydrolysis of phenyl formate to phenol and oxydehydrogenation of PP-ol to PP-one may be relevant to the oxidative photogenerated holes [13]. Also, introducing the $NaIO_3$ as the electron scavenger can decrease the reaction rate of reaction, revealing that photogenerated electrons also play an important role in the C–C bond cleavage of β-O-4 structures. As for C–C bond cleavage in β-1 structure, either hole scavenger or electron scavenger can significantly suppress the conversion of DPol, suggesting that both photogenerated electrons and holes participate in the reaction process of C–C bond cleavage. However, it should be noted that the selectivity for the corresponding products was also affected. More specifically, the selectivity of DPone was unexpectedly increased with the addition of hole scavenger. This result may be owing to that the oxidation of DPol to DPone could also be driven by $O_2^{\bullet-}$ from the reduction of O_2 by photogenerated electrons which could be promoted by providing more photogenerated electrons escape from the recombination with the photogenerated holes [13,19,21,22].

Since the reaction medium is sole acetonitrile, the possibility of hydroxyl radicals acting as the active species could be ruled out [53,54]. The extremely supressed conversion rates of model substrates from the reaction performed under inert gas atmosphere indicated that the participation of O_2 is very important in the fragmentation of C–C bonds. The typical superoxide radical scavenger, p-benzoquinone (p-BQ), was introduced into the reaction system. Interestingly, completely different reaction directions for the C–C bond cleavage in β-O-4 or β-1 structures could be achieved with the addition of p-BQ. It should be noted that the reaction rate of the conversion of PP-ol towards monomeric aromatics

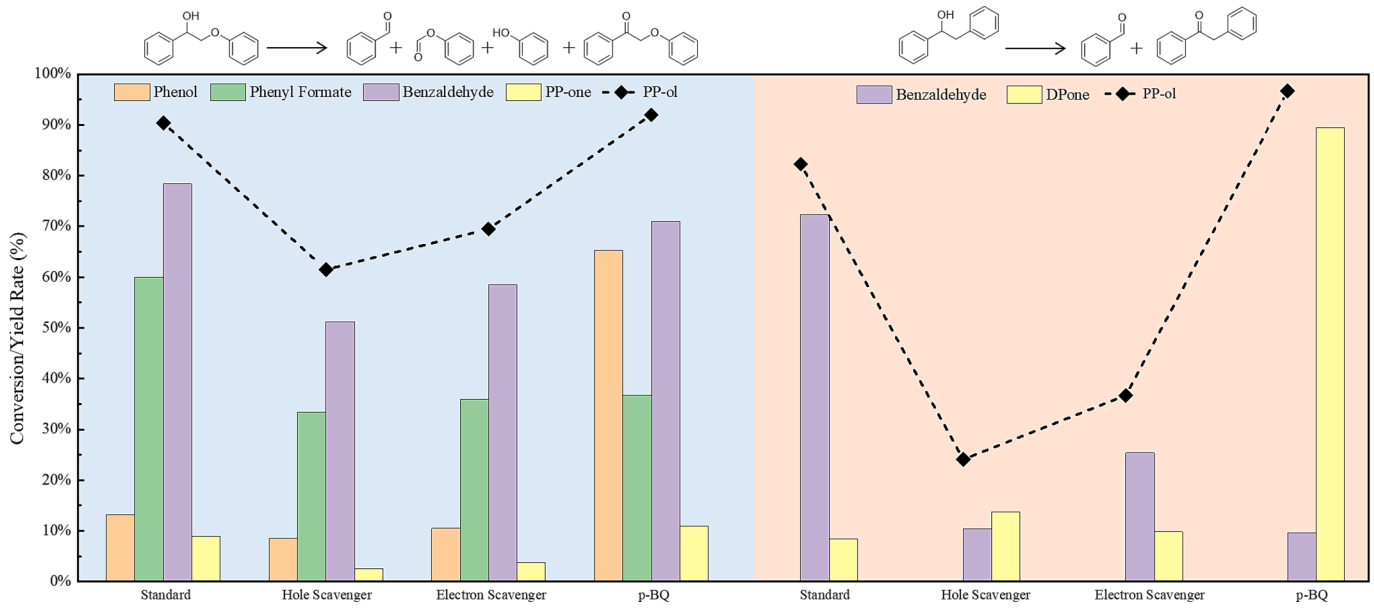

Fig. 5. The control experiments with different additives and reaction substrates. ($Na_2C_2O_4$ was used as the hole scavenger, $NaIO_3$ was used as the electron scavenger, and p-benzoquinone (p-BQ) was used as the superoxide radical scavenger; the reaction time of PP-ol with p-BQ was 1 hr).

was radically improved as similar results could be realised with the reaction time decreased from 5 hr to 1 hr. Also, the yield of phenol from hydrolysis of phenyl formate was significantly increased. Different from some previous studies [23], these results indicate that the oxygen is unlikely to participate the C–C cleavage process in the form of superoxide radical. And the photochemically excited p-BQ can induce oxidation and C–C bond dissociation, which led to the promoted formation of phenol and improved C–C cleavage efficiency [19,55]. However, as for the effect of p-BQ on the DPol conversion, even though the conversion rate still could be remained over 90 % but the selectivity for the oxy-dehydrogenated product of Dpone was dramatically increased, suggesting that the reaction mechanism of C–C cleavage in β-O-4 and β-1 structures could be different and the reactive oxygen species (ROS) originated from the O_2 may play an essential role in the process of C–C bond fragmentation.

Based on the above results, the reaction mechanism of C–C bond cleavage in β-O-4 and β-1 lignin model compounds were respectively proposed as depicted in Scheme 3. Upon the illumination of light, the prepared g-C_3N_4 could be excited and both photogenerated holes and electrons are involved in the reactions. Benefitting from the ultrathin nanosheet morphology, the prepared g-C_3N_4 can exposure more active sites by the enlarged surface area and promote the transfer of photoinduced charge carriers by the shortened migration distance [31,56]. And the cyano group and the vacancies of carbon and nitrogen in the prepared g-C_3N_4 structure not only can improve the separation efficiency and redox potentials of photogenerated charge carriers but also act as

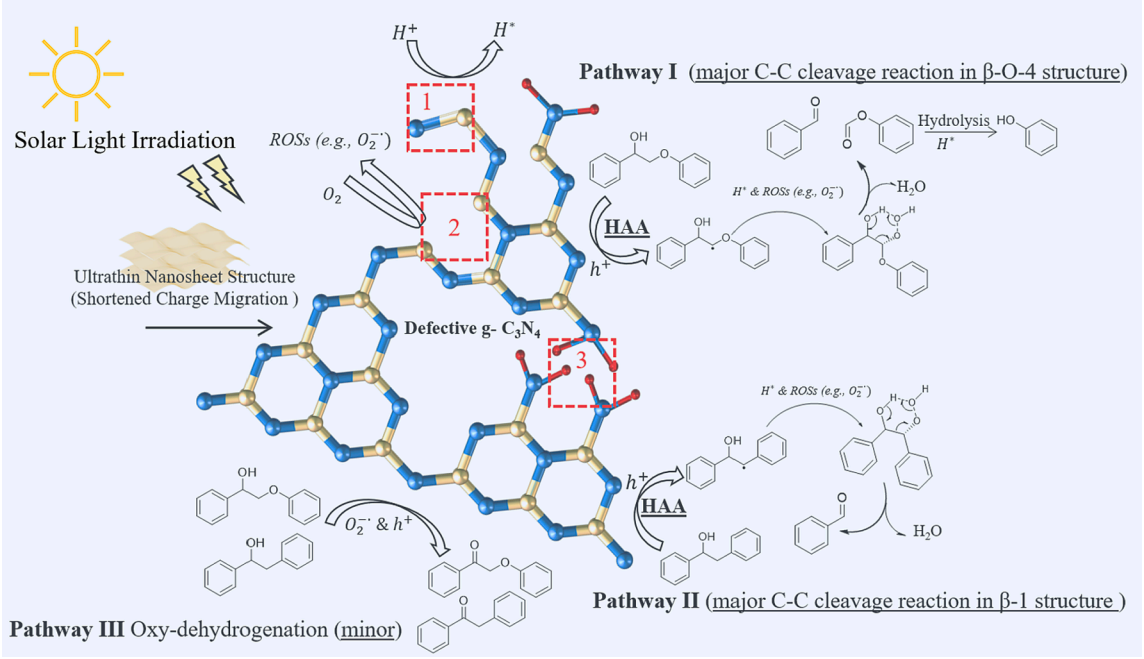

Scheme 3. Proposed mechanism of multi-defective g-C_3N_4 photocatalysed cleavage of C–C bonds in β-O-4 and β-1 structures. (The blue, yellow, and red spheres in the g-C_3N_4 molecular structure sketch represent N, C and H atoms, respectively; and area 1, 2 and 3 represent the –C≡N, N vacancy and C vacancy, respectively).

the active sites for the activation of essential reactive radicals [27,31,56].

More specifically, the initialisation of the conversion reaction of two types of lignin model compounds are similar, both involving the hydrogen atom abstraction (HAA) processes driven by the oxidative photogenerated holes or reactive oxidative species (ROSs). Here, it should be noted that the hydrogen abstracted from the different positions could lead to different subsequent reactions, and thus affecting the selectivity of products. The HAA for the hydroxyl group of C_α-OH or benzylic C_α-H could result in the formation of the corresponding ketone compounds (Pathway III), which is unfavourable to the C–C bond fragmentation due to the increased bond dissociation energy of C_α–C_β bonds [17,18]. The targeting C–C bond fragmentation in β-O-4 and β-1 lignin model compounds only could be efficiently proceeded with the generation of C_β based radicals after deprotonation by the photoinduced holes. Meanwhile, the photogenerated electrons could induce and activate the absorbed oxygen molecules and hydrogen atoms and generate the reactive oxidative species and active hydrogen, respectively [13,19,21,27]. In this case, the absorption and activation of oxygen molecules and hydrogen atoms could be jointly enhanced by the N vacancies and electron-withdrawing cyano group (-C≡N), thus the generation of corresponding reactive radicals could be accelerated and contribute to the formation of reactive radicals and radical intermediates [18,19,26,27]. It should be noted that the step of oxygen molecule activation is very crucial to the overall reaction performance based on the results from the controlled experiments under different atmospheres and with radical scavengers. To further investigate this process, the free energy of oxygen molecule adsorption and activation on the g-C_3N_4 with or without defective structure were calculated through the DFT simulation. The obtained results indicates that the modification of defective sites on g-C_3N_4 can simultaneously reduce the adsorption energy (from 1.048 eV to 0.934 eV) and enhance the interaction between the catalysts and O_2 for electron transfer (from 0.105 eV to 0.204 eV), representing that more oxygen derived radicals could be generated on g-C_3N_4 with multiple defective sites for better catalytic performance. As shown in Pathway I and II, the C_β based radicals may combine with the reactive oxidative species and hydrogen atoms to form peroxide intermediates in the six-membered transitional states by the molecular interactions of hydrogen bonds, π bonds, and σ bonds [18,19,21]. Subsequently, the transition state intermediates are prone to undergo the transfer processes of intramolecular electrons, which could result in the cleavage of C–C bonds and the formation of the corresponding monomeric products with the elimination of H_2O. Due to the strong redox capability of the prepared defective g-C_3N, the formic acid products potentially generated from the C–C bond cleavage in β-O-4 structures could be further transformed to phenolic compounds via hydrolysis process, which further proved the superior redox capability of the catalysts.

4. Conclusion

This study developed the ultrathin graphitic carbon nitride with multiple defects in the structure via a mild synthesis approach using urea and dicyanamide as the precursors. The optimised g-C_3N_4 presented a superior photocatalytic activity for selective C–C bond cleavage in β-O-4 and β-1 types of lignin model compounds. The study of reaction mechanism indicated that the reactive radicals derived from oxygen and both photogenerated holes and electrons play important roles in the reaction process. Herein, the defects structures constructed in the modified g-C_3N_4 can promote the photocatalytic activity for this reaction from two perspectives. From the perspective of materials, the defects can tailor the electronic structures for better separation and transfer of photoinduced charges, thus, the photocatalyst could provide more active photogenerated charge carriers to the reaction. Moreover, from the perspective of reaction kinetics, the generation of essential reactive radicals and radical intermediates could be promoted due to the enhanced absorption and activation on the corresponding vacancies in g-C_3N_4. Apart from the conversion of lignin model compounds, the prepared optimised photocatalyst in this work also showed the promising potential in the conversion of natural lignin biomass and kraft lignin. Overall, this study further revealed the great potential of g-C_3N_4 as the photocatalysts for converting lignin into value-added monomeric aromatics and proposed a promising defects engineering strategy to improve the photocatalytic activity of g-C_3N_4 by modify the electronic structures and providing better active sites.

CRediT authorship contribution statement

Mengyu Cao: Conceptualization, Investigation, Formal analysis, Methodology, Visualization, Writing – original draft, Writing – review & editing. **Shibo Shao:** Conceptualization, Investigation, Validation, Formal analysis, Methodology, Visualization, Writing – original draft, Writing – review & editing. **Wenjing Wei:** Investigation, Formal analysis. **Jason B. Love:** Supervision, Resources. **Zongyang Yue:** Investigation, Formal analysis. **Yiming Zhang:** Investigation, Formal analysis. **Xiaolei Zhang:** Resources, Investigation. **Yuxiang Xue:** Investigation, Validation, Formal analysis. **Jialin Yu:** Investigation, Formal analysis. **Xianfeng Fan:** Conceptualization, Resources, Funding acquisition, Project administration, Supervision, Writing – review & editing.

Declaration of Competing Interest

The authors declare that they have no known competing financial interests or personal relationships that could have appeared to influence the work reported in this paper.

Data availability

No data was used for the research described in the article.

Acknowledgments

X. Fan thank the financial supports from the UK research council EPSRC (EP/WP027593/1; EP/V041665/1). The authors also want to acknowledge Dr. Juraj Bella, Dr. Gary Nichol and Mr. Johnstone Stuart from Chemistry School of the University of Edinburgh and Dr. Sim Gavin, Mr. Casillo Joe and Dr. Nicola Cayzer from Geoscience School of the University of Edinburgh for their strong support and valuable suggestions. S. S want to thank Mr. Fergus Dingwall from Engineering School of the University of Edinburgh for his critical help in this study.

Appendix A. Supplementary data

Supplementary data to this article can be found online at https://doi.org/10.1016/j.apsusc.2023.158653.

References

[1] S. Gazi, Valorization of wood biomass-lignin via selective bond scission: a minireview, Appl. Catal. B Environ. 257 (2019), 117936, https://doi.org/10.1016/j.apcatb.2019.117936.
[2] P. Li, Y. Ouyang, G. Xiao, Y. Zhao, S. Sarina, J. Baeyens, H. Su, H.Y. Zhu, Non-plasmonic Ni nanoparticles catalyzed visible light selective hydrogenolysis of aryl ethers in lignin under mild conditions, Green Chem. 23 (2021) 7780–7789, https://doi.org/10.1039/d1gc01953h.
[3] H. Chen, K. Wan, F. Zheng, Z. Zhang, Y. Zhang, D. Long, Mechanism insight into photocatalytic conversion of lignin for valuable chemicals and fuels production: a state-of-the-art review, Renew. Sustain. Energy Rev. 147 (2021), 111217, https://doi.org/10.1016/j.rser.2021.111217.
[4] S.H. Li, S. Liu, J.C. Colmenares, Y.J. Xu, A sustainable approach for lignin valorization by heterogeneous photocatalysis, Green Chem. 18 (2016) 594–607, https://doi.org/10.1039/c5gc02109j.
[5] J.C. Colmenares, R. Luque, Heterogeneous photocatalytic nanomaterials: Prospects and challenges in selective transformations of biomass-derived compounds, Chem. Soc. Rev. 43 (2014) 765–778, https://doi.org/10.1039/c3cs60262a.

[6] Z. Xiang, W. Han, J. Deng, W. Zhu, Y. Zhang, H. Wang, Photocatalytic conversion of lignin into chemicals and fuels, ChemSusChem 13 (2020) 4199–4213, https://doi.org/10.1002/cssc.202000601.

[7] X. Liu, X. Duan, W. Wei, S. Wang, B.J. Ni, Photocatalytic conversion of lignocellulosic biomass to valuable products, Green Chem. 21 (2019) 4266–4289, https://doi.org/10.1039/c9gc01728c.

[8] M.M. Abu-Omar, K. Barta, G.T. Beckham, J.S. Luterbacher, J. Ralph, R. Rinaldi, Y. Román-Leshkov, J.S.M. Samec, B.F. Sels, F. Wang, Guidelines for performing lignin-first biorefining, Energ. Environ. Sci. 14 (2021) 262–292, https://doi.org/10.1039/d0ee02870c.

[9] L.I. Granone, F. Sieland, N. Zheng, R. Dillert, D.W. Bahnemann, Photocatalytic conversion of biomass into valuable products: a meaningful approach? Green Chem. 20 (2018) 1169–1192, https://doi.org/10.1039/c7gc03522e.

[10] A.J. Ragauskas, G.T. Beckham, M.J. Biddy, R. Chandra, F. Chen, M.F. Davis, B.H. Davison, R.A. Dixon, P. Gilna, M. Keller, P. Langan, A.K. Naskar, J.N. Saddler, T.J. Tschaplinski, G.A. Tuskan, C.E. Wyman, Lignin valorization: improving lignin processing in the biorefinery, Science (80-.) (2014) 344. 10.1126/science.1246843.

[11] M. Zaheer, R. Kempe, Catalytic hydrogenolysis of aryl ethers: A key step in lignin valorization to valuable chemicals, ACS Catal. 5 (2015) 1675–1684, https://doi.org/10.1021/cs501498f.

[12] X. Wu, X. Fan, S. Xie, J. Lin, J. Cheng, Q. Zhang, L. Chen, Y. Wang, Solar energy-driven lignin-first approach to full utilization of lignocellulosic biomass under mild conditions, Nat. Catal. 1 (2018) 772–780, https://doi.org/10.1038/s41929-018-0148-8.

[13] S. Shao, K. Wang, J.B. Love, J. Yu, S. Du, Z. Yue, X. Fan, Water promoted photocatalytic Cβ-O bonds hydrogenolysis in lignin model compounds and lignin biomass conversion to aromatic monomers, Chem. Eng. J. 435 (2022), 134980, https://doi.org/10.1016/j.cej.2022.134980.

[14] C. Zhang, F. Wang, Catalytic lignin depolymerization to aromatic chemicals, Acc. Chem. Res. (2020), https://doi.org/10.1021/acs.accounts.9b00573.

[15] R. Rinaldi, R. Jastrzebski, M.T. Clough, J. Ralph, M. Kennema, P.C.A. Bruijnincx, B. M. Weckhuysen, Paving the way for lignin valorisation: recent advances in bioengineering, biorefining and catalysis, Angew. Chemie - Int. Ed. 55 (2016) 8164–8215, https://doi.org/10.1002/anie.201510351.

[16] L. Dessbesell, M. Paleologou, M. Leitch, R. Pulkki, C. (Charles) Xu, Global lignin supply overview and kraft lignin potential as an alternative for petroleum-based polymers, Renew. Sustain. Energy Rev. 123 (2020), https://doi.org/10.1016/j.rser.2020.109768.

[17] M. Wang, J. Lu, X. Zhang, L. Li, H. Li, N. Luo, F. Wang, Two-step, catalytic C-C bond oxidative cleavage process converts lignin models and extracts to aromatic acids, ACS Catal. 6 (2016) 6086–6090, https://doi.org/10.1021/acscatal.6b02049.

[18] T. Hou, N. Luo, H. Li, M. Heggen, J. Lu, Y. Wang, F. Wang, Yin and Yang dual characters of CuOx clusters for C-C bond oxidation driven by visible light, ACS Catal. 7 (2017) 3850–3859, https://doi.org/10.1021/acscatal.7b00629.

[19] H. Liu, H. Li, J. Lu, S. Zeng, M. Wang, N. Luo, S. Xu, F. Wang, Photocatalytic cleavage of C-C bond in lignin models under visible light on mesoporous graphitic carbon nitride through π-π stacking interaction, ACS Catal. 8 (2018) 4761–4771, https://doi.org/10.1021/acscatal.8b00022.

[20] Y. Wang, J. He, Y. Zhang, CeCl3 -promoted simultaneous photocatalytic cleavage and amination of C α –C β BOND IN LIGNIN MODEL COMPOUNDS AND NATIVE Lignin, CCS Chem. 2 (2020) 107–117, https://doi.org/10.31635/ccschem.020.201900076.

[21] X. Wu, J. Lin, H. Zhang, S. Xie, Q. Zhang, B.F. Sels, Y. Wang, Z-Scheme nanocomposite with high redox ability for efficient cleavage of lignin C-C bonds under simulated solar light, Green Chem. 23 (2021) 10071–10078, https://doi.org/10.1039/d1gc03455c.

[22] D. Liang, J. Wu, C. Xie, J. Wen, Y. Lyu, Z. Sofer, J. Zheng, S. Wang, Efficiently and selectively photocatalytic cleavage of C C bond by C3N4 nanosheets: defect-enhanced engineering and rational reaction route, Appl. Catal. B Environ. 317 (2022), 121690, https://doi.org/10.1016/j.apcatb.2022.121690.

[23] C. Ku, H. Guo, K. Li, Q. Wu, L. Yan, One-step fabrication of mesoporous sulfur-doped carbon nitride for highly selective photocatalytic transformation of native lignin to monophenolic compounds, Chinese Chem. Lett. (2022), https://doi.org/10.1016/j.cclet.2022.03.021.

[24] K. Kumari, P. Choudhary, D. Sharma, V. Krishnan, Amine-functionalized graphitic carbon nitride as a sustainable metal-free catalyst for knoevenagel condensation, Ind. Eng. Chem. Res. 62 (2023) 158–168, https://doi.org/10.1021/acs.iecr.2c03360.

[25] M. Mahdavi, M. Mirmohammadi, M. Baghdadi, S. Mahpishanian, Visible light photocatalytic degradation and pretreatment of lignin using magnetic graphitic carbon nitride for enhancing methane production in anaerobic digestion, Fuel 318 (2022), 123600, https://doi.org/10.1016/j.fuel.2022.123600.

[26] K. Wang, J. Fu, Y. Zheng, Insights into photocatalytic CO2 reduction on C3N4: strategy of simultaneous B, K co-doping and enhancement by N vacancies, Appl. Catal. B Environ. 254 (2019) 270–282, https://doi.org/10.1016/j.apcatb.2019.05.002.

[27] X. Zhang, P. Ma, C. Wang, L. Gan, X. Chen, P. Zhang, Y. Wang, H. Li, L. Wang, X. Zhou, K. Zheng, Unraveling the dual defect sites in graphite carbon nitride for ultra-high photocatalytic H2O2 evolution, Energ. Environ. Sci. 15 (2022) 830–842, https://doi.org/10.1039/d1ee02369a.

[28] S. Li, G. Dong, R. Hailili, L. Yang, Y. Li, F. Wang, Y. Zeng, C. Wang, Effective photocatalytic H2O2 production under visible light irradiation at g-C3N4 modulated by carbon vacancies, Appl. Catal. B Environ. 190 (2016) 26–35, https://doi.org/10.1016/j.apcatb.2016.03.004.

[29] Q. Liang, Z. Li, Z.H. Huang, F. Kang, Q.H. Yang, Holey graphitic carbon nitride nanosheets with carbon vacancies for highly improved photocatalytic hydrogen production, Adv. Funct. Mater. 25 (2015) 6885–6892, https://doi.org/10.1002/adfm.201503221.

[30] Y. Kang, Y. Yang, L.C. Yin, X. Kang, G. Liu, H.M. Cheng, An amorphous carbon nitride photocatalyst with greatly extended visible-light-responsive range for photocatalytic hydrogen generation, Adv. Mater. 27 (2015) 4572–4577, https://doi.org/10.1002/adma.201501939.

[31] S. Gao, X. Wang, C. Song, S. Zhou, F. Yang, Y. Kong, Engineering carbon-defects on ultrathin g-C3N4 allows one-pot output and dramatically boosts photoredox catalytic activity, Appl. Catal. B Environ. 295 (2021), 120272, https://doi.org/10.1016/J.APCATB.2021.120272.

[32] Z. Huang, N. Luo, C. Zhang, F. Wang, Radical generation and fate control for photocatalytic biomass conversion, Nat. Rev. Chem. 6 (2022) 197–214, https://doi.org/10.1038/s41570-022-00359-9.

[33] P. Giannozzi, S. Baroni, N. Bonini, M. Calandra, R. Car, C. Cavazzoni, D. Ceresoli, G.L. Chiarotti, M. Cococcioni, I. Dabo, A. Dal Corso, S. De Gironcoli, S. Fabris, G. Fratesi, R. Gebauer, U. Gerstmann, C. Gougoussis, A. Kokalj, M. Lazzeri, L. Martin-Samos, N. Marzari, F. Mauri, R. Mazzarello, S. Paolini, A. Pasquarello, L. Paulatto, C. Sbraccia, S. Scandolo, G. Sclauzero, A.P. Seitsonen, A. Smogunov, P. Umari, R.M. Wentzcovitch, QUANTUM ESPRESSO: a modular and open-source software project for quantum simulations of materials, J. Phys. Condens. Matter 21 (2009), https://doi.org/10.1088/0953-8984/21/39/395502.

[34] P. Giannozzi, O. Andreussi, T. Brumme, O. Bunau, M. Buongiorno Nardelli, M. Calandra, R. Car, C. Cavazzoni, D. Ceresoli, M. Cococcioni, N. Colonna, I. Carnimeo, A. Dal Corso, S. de Gironcoli, P. Delugas, R.A. DiStasio, A. Ferretti, A. Floris, G. Fratesi, G. Fugallo, R. Gebauer, U. Gerstmann, F. Giustino, T. Gorni, J. Jia, M. Kawamura, H.-Y. Ko, A. Kokalj, E. Küçükbenli, M. Lazzeri, M. Marsili, N. Marzari, F. Mauri, N.L. Nguyen, H.-V. Nguyen, A. Otero-de-la-Roza, L. Paulatto, S. Poncé, D. Rocca, R. Sabatini, B. Santra, M. Schlipf, A.P. Seitsonen, A. Smogunov, I. Timrov, T. Thonhauser, P. Umari, N. Vast, X. Wu, S. Baroni, Advanced capabilities for materials modelling with Quantum ESPRESSO, J. Phys. Condens. Matter 29 (2017), 465901, https://doi.org/10.1088/1361-648X/aa8f79.

[35] J.P. Perdew, K. Burke, M. Ernzerhof, Generalized gradient approximation made simple, Phys. Rev. Lett. 77 (1996) 3865–3868, https://doi.org/10.1103/PhysRevLett.77.3865.

[36] D. Joubert, From ultrasoft pseudopotentials to the projector augmented-wave method, Phys. Rev. B - Condens. Matter Mater. Phys. 59 (1999) 1758–1775, https://doi.org/10.1103/PhysRevB.59.1758.

[37] P.E. Blöchl, Projector augmented-wave method, Phys. Rev. B 50 (1994) 17953–17979, https://doi.org/10.1103/PhysRevB.50.17953.

[38] K. Momma, F. Izumi, VESTA 3 for three-dimensional visualization of crystal, volumetric and morphology data, J. Appl. Cryst. 44 (2011) 1272–1276, https://doi.org/10.1107/S0021889811038970.

[39] M.D. Segall, P.J.D. Lindan, M.J. Probert, C.J. Pickard, P.J. Hasnip, S.J. Clark, M. C. Payne, First-principles simulation: ideas, illustrations and the CASTEP code, J. Phys. Condens. Matter 14 (2002) 2717–2744, https://doi.org/10.1088/0953-8984/14/11/301.

[40] J.W. Steed, Anion-tuned supramolecular gels: a natural evolution from urea supramolecular chemistry, Chem. Soc. Rev. 39 (2010) 3686–3699, https://doi.org/10.1039/b926219a.

[41] X. Yu, S.F. Ng, L.K. Putri, L.L. Tan, A.R. Mohamed, W.J. Ong, Point-defect engineering: leveraging imperfections in graphitic carbon nitride (g-C3N4) photocatalysts toward artificial photosynthesis, Small 17 (2021), https://doi.org/10.1002/smll.202006851.

[42] J. Cheng, Z. Hu, Q. Li, X. Li, S. Fang, X. Wu, M. Li, Y. Ding, B. Liu, C. Yang, L. Wen, Y. Liu, K. Lv, Fabrication of high photoreactive carbon nitride nanosheets by polymerization of amidinourea for hydrogen production, Appl. Catal. B Environ. 245 (2019) 197–206, https://doi.org/10.1016/j.apcatb.2018.12.044.

[43] X. Bao, M. Liu, Z. Wang, D. Dai, P. Wang, H. Cheng, Y. Liu, Z. Zheng, Y. Dai, B. Huang, Photocatalytic selective oxidation of HMF coupled with H 2 evolution on flexible ultrathin g-C 3 N 4 nanosheets with enhanced N-H interaction, ACS Catal. (2022) 1919–1929, https://doi.org/10.1021/acscatal.1c05357.

[44] W. Li, Z. Wei, K. Zhu, W. Wei, J. Yang, J. Jing, D.L. Phillips, Y. Zhu, Nitrogen-defect induced trap states steering electron-hole migration in graphite carbon nitride, Appl. Catal. B Environ. 306 (2022), 121142, https://doi.org/10.1016/j.apcatb.2022.121142.

[45] Q. You, C. Zhang, M. Cao, B. Wang, J. Huang, Y. Wang, S. Deng, G. Yu, Defects controlling, elements doping, and crystallinity improving triple-strategy modified carbon nitride for efficient photocatalytic diclofenac degradation and H2O2 production, Appl. Catal. B Environ. 321 (2022), 121941, https://doi.org/10.1016/j.apcatb.2022.121941.

[46] D. Zhao, C.L. Dong, B. Wang, C. Chen, Y.C. Huang, Z. Diao, S. Li, L. Guo, S. Shen, Synergy of dopants and defects in graphitic carbon nitride with exceptionally modulated band structures for efficient photocatalytic oxygen evolution, Adv. Mater. 31 (2019), https://doi.org/10.1002/adma.201903545.

[47] D. Zhu, Q. Zhou, Nitrogen doped g-C3N4 with the extremely narrow band gap for excellent photocatalytic activities under visible light, Appl. Catal. B Environ. 281 (2021), 119474, https://doi.org/10.1016/j.apcatb.2020.119474.

[48] F. Dong, Z. Wang, Y. Sun, W.K. Ho, H. Zhang, Engineering the nanoarchitecture and texture of polymeric carbon nitride semiconductor for enhanced visible light photocatalytic activity, J. Colloid Interface Sci. 401 (2013) 70–79, https://doi.org/10.1016/j.jcis.2013.03.034.

[49] H. Zhao, Q. Jin, M.A. Khan, S. Larter, S. Siahrostami, M.G. Kibria, J. Hu, Rational design of carbon nitride for remarkable photocatalytic H2O2 production, Chem Catal. 2 (2022) 1720–1733, https://doi.org/10.1016/j.checat.2022.04.015.

[50] J. Zhang, M. Zhang, R.Q. Sun, X. Wang, A facile band alignment of polymeric carbon nitride semiconductors to construct isotype heterojunctions, Angew. Chemie - Int. Ed. 51 (2012) 10145–10149, https://doi.org/10.1002/anie.201205333.
[51] C. Feng, L. Tang, Y. Deng, J. Wang, J. Luo, Y. Liu, X. Ouyang, H. Yang, J. Yu, J. Wang, Synthesis of leaf-vein-like g-C3N4 with tunable band structures and charge transfer properties for selective photocatalytic H2O2 evolution, Adv. Funct. Mater. 30 (2020) 1–13, https://doi.org/10.1002/adfm.202001922.
[52] Z. Qin, Z. Huang, M. Wang, D. Liu, Y. Chen, L. Guo, Synergistic effect of quantum confinement and site-selective doping in polymeric carbon nitride towards overall water splitting, Appl. Catal. B Environ. 261 (2020), 118211, https://doi.org/10.1016/j.apcatb.2019.118211.
[53] X. Cao, Z. Chen, R. Lin, W.C. Cheong, S. Liu, J. Zhang, Q. Peng, C. Chen, T. Han, X. Tong, Y. Wang, R. Shen, W. Zhu, D. Wang, Y. Li, A photochromic composite with enhanced carrier separation for the photocatalytic activation of benzylic C-H bonds in toluene, Nat. Catal. 1 (2018) 704–710, https://doi.org/10.1038/s41929-018-0128-z.
[54] K. Su, H. Liu, B. Zeng, Z. Zhang, N. Luo, Z. Huang, Z. Gao, F. Wang, Visible-light-driven selective oxidation of toluene into benzaldehyde over nitrogen-modified Nb2O5 nanomeshes, ACS Catal. 10 (2020) 1324–1333, https://doi.org/10.1021/acscatal.9b04215.
[55] L.J. Mitchell, C.J. Moody, Solar photochemical oxidation of alcohols using catalytic hydroquinone and copper nanoparticles under oxygen: Oxidative cleavage of lignin models, J. Org. Chem. 79 (2014) 11091–11100, https://doi.org/10.1021/jo5020917.
[56] V.W. Hei Lau, V.W. Zhe Yu, F. Ehrat, T. Botari, I. Moudrakovski, T. Simon, V. Duppel, E. Medina, J.K. Stolarczyk, J. Feldmann, V. Blum, B.V. Lotsch, Urea-modified carbon nitrides: enhancing photocatalytic hydrogen evolution by rational defect engineering, Adv. Energy Mater. 7 (2017) 1–15, https://doi.org/10.1002/aenm.201602251.